Optics Letters

Rapid wide-field Mueller matrix polarimetry imaging based on four photoelastic modulators with no moving parts

Sanaz Alali,[1,†] Adam Gribble,[2,*,†] and I. Alex Vitkin[2,3,4]

[1]Wellman Center for Photomedicine, Harvard Medical School, 40 Blossom Street, Boston, Massachusetts 02114, USA
[2]Department of Medical Biophysics, University of Toronto, 101 College Street, Toronto, Ontario M5G 2M9, Canada
[3]Division of Biophysics and Bioimaging, Princess Margaret Cancer Centre, University Health Network, 610 University Avenue, Toronto, Ontario M5G 2M9, Canada
[4]Department of Radiation Oncology, University of Toronto, 610 University Avenue, Toronto, Ontario M5G 2M9, Canada
*Corresponding author: adam.gribble@mail.utoronto.ca

Received 26 October 2015; accepted 24 November 2015; posted 16 December 2015 (Doc. ID 252483); published 29 February 2016

A new polarimetry method is demonstrated to image the entire Mueller matrix of a turbid sample using four photoelastic modulators (PEMs) and a charge coupled device (CCD) camera, with no moving parts. Accurate wide-field imaging is enabled with a field-programmable gate array (FPGA) optical gating technique and an evolutionary algorithm (EA) that optimizes imaging times. This technique accurately and rapidly measured the Mueller matrices of air, polarization elements, and turbid phantoms. The system should prove advantageous for Mueller matrix analysis of turbid samples (e.g., biological tissues) over large fields of view, in less than a second.

OCIS codes: (120.5410) Polarimetry; (170.4090) Modulation techniques; (260.5430) Polarization; (230.4110) Modulators.

http://dx.doi.org/10.1364/OL.41.001038

Polarized light is used for metrology in many areas such as aerosol detection, semiconductor wafer inspection, and biomedicine. The most complete polarimetry methodology is to measure a sample's 16-element (4 × 4) Mueller matrix, a polarization transfer function that describes its interaction with (fully or partially) polarized light. Mathematically, $\vec{S}_{\text{out}} = \mathbf{M}\vec{S}_{\text{in}}$, with $\mathbf{M}$ the Mueller matrix, and $\vec{S}_{\text{in}}$ and $\vec{S}_{\text{out}}$ Stokes vectors that describe light polarization before and after sample interaction. Stokes vectors contain four elements, $\vec{S} = [i \quad q \quad u \quad v]^T$, where i is light intensity, q describes horizontal and vertical polarization, u describes +45° and −45° polarization, and v describes circular polarization. A sample's Mueller matrix contains information about structure and composition, often expressed as depolarization, retardance, or optical rotation. In biomedicine, optical rotations reveal glucose levels in turbid media [1,2]; linear retardances in *ex-vivo* rat myocardia reveal structural damage and regeneration with stem-cell therapy [1,3]; changes in bladder wall morphology due to outlet obstruction are localized [4]; and depolarization correlates with cancer grade in human cervix [5] and colon [6,7], and radiofrequency ablation lesion extent in the heart [8].

Mueller matrix elements of an unknown turbid sample are independent, thus full determination requires at least 16 polarimetric measurements. The simplest technique is mechanical alterations of polarization elements before and after a sample. However, this is time-consuming and prone to random and systematic errors, a low SNR scenario undesirable for thick turbid heterogeneous samples. Further, long measurements increase sensitivity to sample motion artifacts.

Polarimetry has seen many recent advances to measure the Mueller matrices of turbid media with improved accuracy and speed. Snapshot polarimeters, based on diffractive components, encode and detect polarizations via spatial frequency filters, use no moving parts, and are the fastest Mueller imagers; however, images are subject to artifacts and information loss due to spatial filtering [9]. Another approach is to replace static polarization optics with switchable or dynamic ones. For example, switchable liquid crystals (LCs) can measure Mueller matrices in seconds [7,10,11]. This study used photoelastic modulators (PEMs, Hinds Instruments), which are superior to LCs in modulation efficiency and clear aperture size (15–30 mm, frequency dependent) [12]. Fast, accurate polarization modulation enables quick, sensitive Mueller matrix determination. The PEMs' piezoelectric transducers induce rapid birefringence modulation in isotropic crystals (e.g., silica) via the photoelastic effect. Light traversing the crystal acquires variable retardance, $\delta_i(t)$, at its resonance frequency (20–100 kHz), f_i:

$$\delta_i(t) = \delta_{0i} \sin(2\pi f_i t + \varphi_i), \tag{1}$$

where δ_{0i} is amplitude and φ_i is phase (0 to 2π). Amplitudes are user controlled, but PEM relative phases are initially unknown. Rapid retardance modulations are well-suited for sensitive measurements, since signal oscillations recorded by a point detector (e.g., photodiode) can be sensitively demodulated via synchronous lock-in detection at PEM frequencies (or harmonics). Such nonimaging schemes are suitable for point sensing or point scanning to slowly form images. To enable wide-field

imaging with comparably high SNR, imaging detectors (e.g., CCD camera) with alternative synchronization gating are needed.

Previously, we reported a simpler two-PEM system able to image Stokes vectors (polarizations) of light with a CCD and field programmable gate array (FPGA)-assisted sequential gating [13]. Unknown Stokes vectors were imaged in 80 ms, with no moving parts or beam steering. However, to characterize a turbid sample, its full Mueller matrix must be imaged. We recently proposed a solution using four PEMs [14]. Here, a working four-PEM Mueller matrix imaging system is revealed.

The imaging system is depicted in Fig. 1(a). Laser light (641 nm, Coherent Cube) passed through a polarization state generator (PSG) of linear polarizer (0° to vertical) and two PEMs. The polarizer determined the input polarization, $\vec{S}_{\text{in}} = [1 \quad 1 \quad 0 \quad 0]^T$. PEMs are described by time-varying Mueller matrices [$\mathbf{M}_{\text{PEM}i}(t)$ for $i = 1$ to 4] of theoretical retarders [15] with amplitude $\delta_i(t)$ and fast axis θ_i. PEM properties in the PSG were $f_1 = 50$ kHz, $\theta_1 = 45°$; $f_2 = 20$ kHz, and $\theta_2 = 90°$. After interaction with a sample of Mueller matrix $\mathbf{M}$, light traversed a polarization state analyzer (PSA) consisting of two PEMs ($f_3 = 47$ kHz, $\theta_3 = -45°$; $f_4 = 42$ kHz, $\theta_4 = 90°$) and a polarizer (45°, $\mathbf{M}_{P2}$) before reaching a CCD camera (PIMAX-3, Princeton Instruments). Camera acquisition was triggered by an FPGA (Altera DE2).

Similar to [14], polarization reaching the CCD is time-variant, due to dynamic PEM birefringences, and is found by multiplication of PSG, PSA, and sample Mueller matrices:

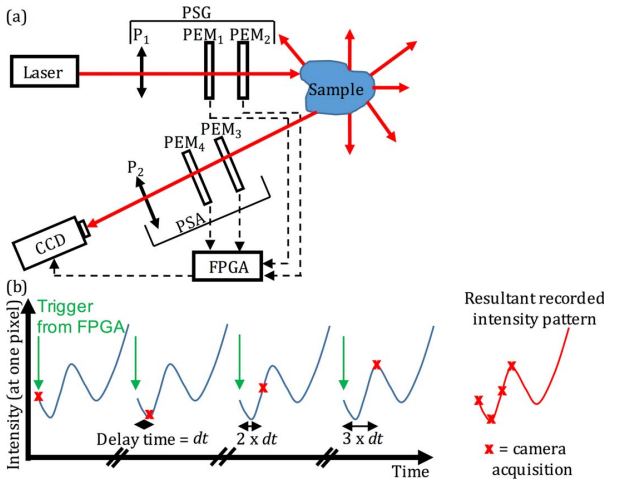

Fig. 1. Four-PEM Mueller matrix imaging system. (a) Laser light passed through a polarization state generator (PSG) of polarizer (P_1, 0°) and two photoelastic modulators (PEMs; 50 kHz, 45°; 20 kHz, 90°). After sample interaction, output polarization traversed a polarization state analyzer (PSA) of two PEMs (47 kHz, −45°; 42 kHz, 90°) and polarizer (P_2, 45°). A time-varying intensity reached a CCD. Lenses can be added to adjust resolution and field-of-view. A field-programmable gate array (FPGA) triggered CCD acquisition based on PEM reference frequencies. (b) The FPGA ensured each sequential image acquisition was triggered at the same PEM phase relationship. That is, when the FPGA detected a unique phase relationship between PEM reference frequencies, a trigger was sent to the CCD, and an image recorded (red cross). When the CCD was ready to image again, acquisition was delayed by $dt = 0.5$ μs relative to the FPGA-sent trigger. Delay time increased with each successive image, enabling image acquisition of the entire modulation of the four-PEM system. For simplicity, acquisition at one pixel is illustrated.

$$\vec{S}_{\text{out}}(t) = \mathbf{M}_{P2}\mathbf{M}_{\text{PEM4}}(t)\mathbf{M}_{\text{PEM3}}(t)\mathbf{M}\mathbf{M}_{\text{PEM2}}(t)\mathbf{M}_{\text{PEM1}}(t)\vec{S}_{\text{in}}. \tag{2}$$

After multiplying PSG/PSA matrices, intensity at the CCD is

$$i(t) = \vec{A}(t)\mathbf{M}\vec{G}(t). \tag{3}$$

$\vec{G}(t) = [g_1(t) \quad g_2(t) \quad g_3(t) \quad g_4(t)]^T = \mathbf{M}_{\text{PEM2}}(t)\mathbf{M}_{\text{PEM1}}(t)\vec{S}_{\text{in}}$ is a PSG dependent, time-varying input Stokes vector. $\vec{A}(t) = [a_1(t) \quad a_2(t) \quad a_3(t) \quad a_4(t)]$ is PSA dependent (first row of $\mathbf{M}_{P2}\mathbf{M}_{\text{PEM4}}(t)\mathbf{M}_{\text{PEM3}}(t)$). Equation (3) can be written:

$$i(t) = \vec{Z}(t)\vec{M}, \tag{4}$$

with $\vec{Z}(t)$ a 16-element row vector determined by PSG and PSA:

$$\begin{aligned}\vec{Z}(t) &= [z_1(t) \quad z_2(t) \quad \cdots \quad z_{16}(t)] \\ &= [a_1(t)g_1(t) \quad a_1(t)g_2(t) \quad a_1(t)g_3(t) \quad a_1(t)g_4(t) \\ &\quad \cdots \quad a_4(t)g_1(t) \quad a_4(t)g_2(t) \quad a_4(t)g_3(t) \quad a_4(t)g_4(t)],\end{aligned} \tag{5}$$

and $\vec{M}$ the sample Mueller matrix as a 16×1 column vector

$$\vec{M}^T = [m_{11} \quad m_{12} \quad m_{13} \quad m_{14} \; m_{21} \quad \cdots \quad m_{44}], \tag{6}$$

where m_{ij} denotes the i^{th}, j^{th} element of $\mathbf{M}$.

To recover $\vec{M}$, ≥16 linear equations are created by recording CCD intensities at $N \geq 16$ time points, $i(t_i)$ (for $i = 1$ to N):

$$[i(t_1) \quad i(t_2) \quad \cdots \quad i(t_N)]^T = \mathbf{Z}\vec{M}, \tag{7}$$

where the vector on the left contains intensities from $N \geq 16$ time points. $\mathbf{Z}$ is an $N \times 16$ "system matrix" determined by the PSG and PSA optics at each time point. It is defined as

$$\mathbf{Z} = \begin{bmatrix} \vec{Z}(t_1) \\ \vdots \\ \vec{Z}(t_N) \end{bmatrix} = \begin{bmatrix} z_1(t_1) & \cdots & z_{16}(t_1) \\ \vdots & \ddots & \vdots \\ z_1(t_N) & \cdots & z_{16}(t_N) \end{bmatrix}. \tag{8}$$

If $\mathbf{Z}$ is invertible, the Mueller matrix is found as

$$\vec{M} = \mathbf{Z}^{-1}[i(t_1) \quad i(t_2) \quad \cdots \quad i(t_N)]^T. \tag{9}$$

$\mathbf{Z}^{-1}$ is the inverse system matrix. If $N > 16$, $\mathbf{Z}$ is overdetermined and its pseudoinverse is used for Mueller recovery.

To ensure a stable solution of $\vec{M}$, $\mathbf{Z}$ must be nonsingular and stable in the presence of measurement errors. One method is to select a system matrix with low condition number [16], $\kappa(\mathbf{Z})$, the ratio of largest to smallest singular values. Minimizing $\kappa(\mathbf{Z})$ effectively minimizes recovery error in $\vec{M}$ with respect to measurement errors in $i(t_i)$ [16]. To use time points that generate low $\kappa(\mathbf{Z})$, enabling robust Mueller recovery through Eq. (9), it is first necessary to set accurate imaging times and measure exact PEM parameters.

To ensure accurate timing of image acquisition, the previously exhibited FPGA-assisted time gating methodology with two PEMS and a CCD [13] was extended to four PEMs. Briefly, a 32 bit, 50 MHz FPGA counted rising edges of each PEM modulation signal and locked onto a unique phase relation between all four PEMs (i.e., unique integer count of rising edges for each PEM, within a short time). When this relation occurred (within 60 ns error), the FPGA sent a trigger to the CCD to gate intensity for 0.5 μs. CCD image acquisition took approximately 20 ms. To enable sequential gating, CCD gating was delayed in

each sequential image by 0.5 μs multiples. This allowed imaging a half period of the 4-PEM modulation (500 out of 1000 μs), despite PEMs going through multiple periods. For example, image 1000 was recorded after a 500 μs (1000 × 0.5 μs) delay. The acquisition scheme is depicted in Fig. 1(b).

To estimate the PEM phases, a similar calibration procedure to [13] was followed, using three samples with known Muller matrices (hereafter referred to as "calibration samples"): blank (air), polarizer (45°), and quarter-wave plate (QWP, 0°). Transmission geometry was used, but the setup could be extended to reflection [as per Fig. 1(a)]. For each sample, images at 1000 time points, evenly spaced from $t = 0$ to 500 μs (half period of PSG/PSA modulation), were recorded with the CCD. The center 3 × 3 pixel area of each image was averaged to generate experimental intensity versus time plots (Fig. 2). An evolutionary algorithm (EA) [17] was then used to find the PEM phases. Briefly, the EA started with a random set of PEM phases (parents), which evolved by iterating combinations of two operators: asexual and sexual mutations [17]. After each iteration, the sets of PEM phases were used to simulate intensity patterns for each calibration sample, via Eq. (3) (along with known PSG/PSA parameters, see Fig. 1, and ideal sample Mueller matrices, Table 2). For each set of PEM phases, the correlation between simulated and experimental intensity patterns was calculated for all three calibration samples, and these correlations were averaged. The set of phases that maximized this average correlation survived to generate more candidate sets (offspring). The EA was run until correlation was high and no longer increasing. This yielded PEM phases $\varphi_1 = 325.4°$, $\varphi_2 = 338.0°$, $\varphi_3 = 63.60°$, and $\varphi_4 = 297.4°$.

To demonstrate the calibration efficacy, intensity patterns for a blank (air) sample are shown in Fig. 2(a). Excellent agreement is seen between experiment and simulation with EA derived PEM phases (correlation =0.9936). Similar results were found for "noncalibration" samples (not used to find PEM phases) [e.g., 45° QWP, Fig. 2(b)]. All results are in Table 1.

Once PEM parameters were known, a new EA was used to find a subset of imaging times that minimized the condition number of $\mathbf{Z}$ (giving $\kappa(\mathbf{Z}) = 3.43$). An overdetermined system matrix ($N = 50$ versus the minimum 16) was used to further limit sensitivity to measurement errors. More time points could be used but with increased imaging time; 50 time points offered balance between speed (~1 s) and accuracy in Mueller matrix recovery. The acquisition can be adjusted so only these optimal time points (t_i to t_{50}) are imaged, as opposed to all 1000 used to find PEM phases.

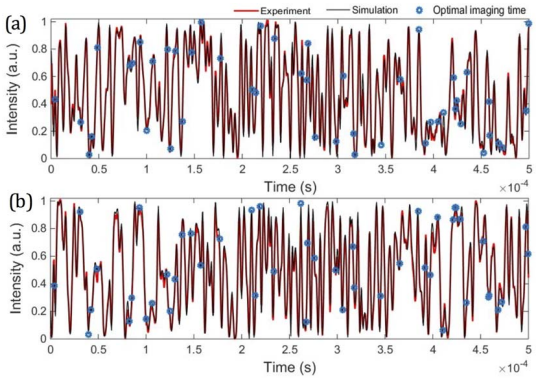

Fig. 2. Experimental (red) versus simulated (black) intensity patterns of the four-PEM system, using PEM phases found by calibration. (a) Blank (air) sample used for PEM phase calibration; correlation =0.9936. (b) QWP at 45°, not used for calibration; correlation =0.9951. Blue circles show the 50 time points for optimal Mueller recovery.

Table 1. Summary of PEM Calibration

Sample	Correlation Coefficient (Experimental versus Simulated Intensity Patterns)
Blank[a]	0.9936
Polarizer (45°)[a]	0.9966
QWP (0°)[a]	0.9932
Polarizer (0°)[b]	0.9951
QWP (45°)[b]	0.9932

[a]"Calibration" samples—used to find the PEM phases
[b]"Noncalibration samples—not used to find PEM phases

Using experimentally determined PEM phases and optimal time points, system matrix $\mathbf{Z}$ was derived and used for Mueller matrix recovery, via Eq. (9). Recovered Mueller matrices for calibration and unknown samples are in Table 2, and two representative images are in Fig. 3. Spatial variance from the center may be due to photons that passed through the PEMs at off-axis angles, acquiring slightly different retardances. To evaluate performance, differences between theoretical and experimental Mueller matrices were calculated (Table 2). The largest error in any matrix element, for all five samples, was 0.073 (M_{44} of 45° QWP). These minor differences between theory and

Table 2. Summary of Mueller Matrix Recovery

Theoretical Mueller Matrix	Experimental Mueller Matrix (Averaged over Image)	Mueller Matrix Element Error	
		Mean	Max
Blank[a]			
1 0 0 0	1.000 0.006 0.007 0.017	0.015	0.036
0 1 0 0	0.010 0.976 −0.019 0.003		
0 0 1 0	0.002 −0.018 1.00 0.018		
0 0 0 1	0.036 0.032 −0.020 0.976		
Polarizer (45°)[a]			
1 0 1 0	1.000 0.023 0.971 0.006	0.022	0.050
0 0 0 0	0.031 0.022 0.050 0.022		
1 0 1 0	0.963 0.018 0.968 0.038		
0 0 0 0	−0.001 0.013 −0.012 −0.013		
QWP (0°)[a,c]			
1 0 0 0	1.000 −0.001 0.000 −0.006	0.016	0.049
0 1 0 0	−0.012 0.960 0.036 −0.011		
0 0 −0.052 0.999	−0.001 0.015 −0.076 0.980		
0 0 −0.999 −0.052	0.019 0.013 −0.950 −0.048		
Polarizer (0°)[b]			
1 1 0 0	1.000 0.980 −0.011 −0.001	0.021	0.056
1 1 0 0	0.944 0.944 −0.004 −0.024		
0 0 0 0	0.002 −0.010 −0.038 −0.008		
0 0 0 0	0.042 0.022 −0.007 0.041		
QWP (45°)[b,c]			
1 0 0 0	1.000 0.024 −0.006 0.007	0.019	0.073
0 −0.052 0 −0.999	0.002 −0.113 −0.046 −1.005		
0 0 1 0	0.019 0.010 1.006 0.002		
0 0.999 0 −0.052	−0.002 0.971 0.007 −0.125		

[a]"Calibration" samples—used to find the PEM phases
[b]"Noncalibration" samples—not used to find PEM phases
[c]QWP had 93° retardance at 641 nm, thus deviates from 1 s and 0 s

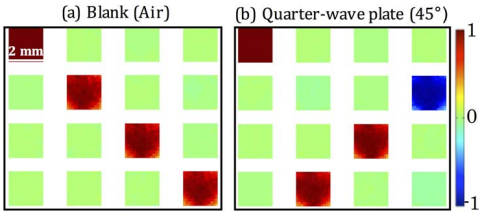

Fig. 3. Mueller matrix images of (a) a blank (air) sample used for PEM phase calibration and (b) a 45° QWP (unknown "noncalibration" sample), as found with the four-PEM Mueller matrix imaging system. See Table 2 for average (and theoretical) values.

experiment may be due to several factors, such as imperfect polarization elements. Further, relative PEM phases are only correct to the precision of the FPGA counter. Finally, depolarization and reflections (if any) of system components may cause slight artifacts. These will be investigated in the future.

To demonstrate the capability of the system for arbitrary sample analysis, a thick ($d = 4$ mm) turbid birefringent biological phantom (elastic polyacrylamide polymer) [18] was synthesized and imaged. When stretched, these phantoms exhibit birefringence, Δn, along the axis of strain ($\Delta n = 4.1 \times 10^{-5}$ per mm of extension [2]). Turbidity ($\mu_s = 6$ cm^{-1} from Mie theory [19,20]) was created with polystyrene microsphere scatterers (0.96 μm diameter, refractive index =1.59, Bangs Laboratories). The four-PEM system was used to image the Mueller matrix of the phantom when unstretched and following 4 mm of stretch directed along the 90° axis [Figs. 4(a)–4(b)]. Polar decomposition [21] was used to reveal the depth-integrated effect of birefringence, namely linear retardance. Retardance images are shown in Figs. 4(c)–4(d). Prior to being stretched, the phantom exhibited a "background" mean linear retardance magnitude of 8.4°. This nonzero retardance is due to background strain exerted by the stretching mount. After stretching, the retardance was 47.4° oriented at 93°. This increase in retardance with 4 mm of stretch (47.4°–8.4° = 39.0°) agrees well with the prediction ($\delta = (2\pi/\lambda)\Delta nd = 35.6°$), as does the retardance direction (93°).

As we previously described [14], many configurations of the four-PEM polarimetry system are possible. PEM orientations, PEM retardance amplitudes, and PSG/PSA polarizer orientations can be adjusted. PEM frequencies can also be adjusted,

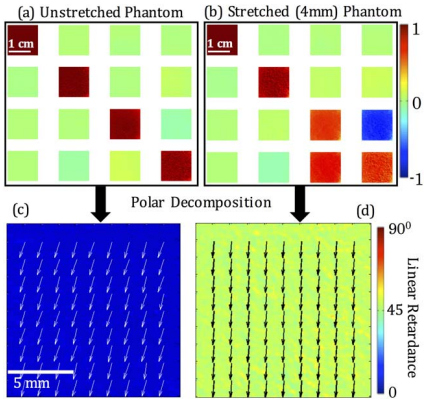

Fig. 4. Mueller matrix images of (a) unstretched and (b) stretched turbid birefringent polyacrylamide phantoms, and (c), (d) respective linear retardances found via polar decomposition. Arrows show retardance direction. Measured retardances agree well with theory.

although discretely, with less flexibility. It may be possible to improve sensitivity by selecting these parameters to further minimize the condition number of the system matrix. Other potential improvements include optimization of CCD integration time, increased sampling rate to improve estimation of PEM phases, and increased averaging to reduce random noise. A full study on error sources will be done in the future. Imaging speed is limited by CCD image acquisition, approximately 20 ms. Mueller matrix recovery with 50 images thus takes about 1 s of total imaging time. System improvements may permit as few as 16 images (320 ms) for Mueller matrix recovery. At these rates there is potential for dynamic, near-real-time Mueller matrix imaging (1–3 frames per second).

In summary, a rapid PEM-based wide-field Mueller matrix imaging system with high SNR has been demonstrated to image arbitrary turbid samples, with no moving parts, large field of view, and no degradation due to spatial filtering. Future work will quantify and reduce error sources and extend the platform to biological tissue analysis.

[†]These authors contributed equally to this work.

Funding. Natural Sciences and Engineering Research Council of Canada (NSERC).

REFERENCES

1. N. Ghosh, M. F. G. Wood, S. Li, R. D. Weisel, B. C. Wilson, R.-K. Li, and I. A. Vitkin, J. Biophoton. **2**, 145 (2009).
2. M. F. G. Wood, X. Guo, and I. A. Vitkin, J. Biomed. Opt. **12**, 014029 (2007).
3. M. F. G. Wood, N. Ghosh, M. A. Wallenburg, S.-H. Li, R. D. Weisel, B. C. Wilson, R.-K. Li, and I. A. Vitkin, J. Biomed. Opt. **15**, 047009 (2010).
4. S. Alali, K. J. Aitken, A. Schröder, A. Gribble, D. J. Bagli, and I. A. Vitkin, Biomed. Opt. Express **5**, 621 (2014).
5. A. Pierangelo, A. Nazac, A. Benali, P. Validire, H. Cohen, T. Novikova, B. H. Ibrahim, S. Manhas, C. Fallet, M.-R. Antonelli, and A. De Martino, Opt. Express **21**, 14120 (2013).
6. A. Pierangelo, S. Manhas, A. Benali, C. Fallet, M.-R. Antonelli, T. Novikova, B. Gayet, P. Validire, and A. De Martino, J. Biomed. Opt. **17**, 066009 (2012).
7. A. Pierangelo, S. Manhas, A. Benali, C. Fallet, J.-L. Totobenazara, M.-R. Antonelli, T. Novikova, B. Gayet, A. De Martino, and P. Validire, J. Biomed. Opt. **18**, 046014 (2013).
8. I. Ahmad, A. Gribble, M. Ikram, M. Pop, and A. Vitkin, "Polarimetric assessment of healthy and radio frequency ablated porcine myocardial tissue," J. Biophoton. (to be published).
9. M. W. Kudenov, M. J. Escuti, N. Hagen, E. L. Dereniak, and K. Oka, Opt. Lett. **37**, 1367 (2012).
10. P. A. Letnes, I. S. Nerbø, L. M. S. Aas, P. G. Ellingsen, and M. Kildemo, Opt. Express **18**, 23095 (2010).
11. E. Garcia-Caurel, A. De Martino, and B. Drévillon, Thin Solid Films **455–456**, 120 (2004).
12. O. Arteaga, J. Freudenthal, B. Wang, and B. Kahr, Appl. Opt. **51**, 6805 (2012).
13. S. Alali, T. Yang, and I. A. Vitkin, Opt. Lett. **38**, 2997 (2013).
14. S. Alali and I. A. Vitkin, Opt. Eng. **52**, 103114 (2013).
15. D. H. Goldstein, *Polarized Light*, 3rd ed. (CRC Press, 2011).
16. K. M. Twietmeyer and R. A. Chipman, Opt. Express **16**, 11589 (2008).
17. F. Massoumian, S. Alali, and T. Mansouri, Opt. Lett. **34**, 67 (2009).
18. A. Surowiec, P. N. Shrivastava, M. Astrahan, and Z. Petrovich, Int. J. Hyperthermia **8**, 795 (1992).
19. H. C. van de Hulst, *Light Scattering by Small Particles* (Dover, 1981).
20. S. Prahl, "Mie Scattering Calculator," http://omlc.ogi.edu/calc/mie_calc.html.
21. S.-Y. Lu and R. A. Chipman, J. Opt. Soc. Am. **13**, 1106 (1996).